Characterization of low-loss hydrogenated amorphous silicon films for superconducting resonators

Bruno T. Buijtendorp,[a,*] **Juan Bueno**,[a,b] **David J. Thoen**,[a] **Vignesh Murugesan**,[b] **Paolo M. Sberna**,[a] **Jochem J. A. Baselmans**,[a,b] **Sten Vollebregt**,[a] **and Akira Endo**[a]

[a]Delft University of Technology, Faculty of Electrical Engineering, Mathematics and Computer Science, Delft, The Netherlands

[b]SRON – Netherlands Institute for Space Research, Leiden, The Netherlands

Abstract. Superconducting circuit elements used in millimeter-submillimeter (mm-submm) astronomy would greatly benefit from deposited dielectrics with small dielectric loss and noise. This will enable the use of multilayer circuit elements and thereby increase the efficiency of mm-submm filters and allow for a miniaturization of microwave kinetic inductance detectors (MKIDs). Amorphous dielectrics introduce excess loss and noise compared with their crystalline counterparts, due to two-level system defects of unknown microscopic origin. We deposited hydrogenated amorphous silicon films using plasma-enhanced chemical vapor deposition, at substrate temperatures of 100°C, 250°C, and 350°C. The measured void volume fraction, hydrogen content, microstructure parameter, and bond-angle disorder are negatively correlated with the substrate temperature. All three films have a loss tangent below 10^{-5} for a resonator energy of 10^5 photons, at 120 mK and 4 to 7 GHz. This makes these films promising for MKIDs and on-chip mm-submm filters. [DOI: 10.1117/1.JATIS.8.2.028006]

Keywords: kinetic inductance detectors; filter bank; spectrometer; millimeter-submillimeter; amorphous silicon; dielectric loss.

Paper 21150G received Nov. 26, 2021; accepted for publication May 13, 2022; published online Jun. 10, 2022.

1 Introduction

The integrated superconducting spectrometer (ISS)[1–3] is a novel astronomical instrument that promises ultra-wideband, high-sensitivity, and three-dimensional imaging spectrometry in the millimeter-submillimeter (mm-submm) band. ISSs enable large arrays of spectroscopic pixels because they are intrinsically scalable due to the compact on-chip filterbank for signal dispersion and because they allow for frequency-domain multiplexed readout of the microwave kinetic inductance detectors (MKIDs).[4]

Currently, the DESHIMA[3] ISS has a planar design using coplanar waveguide (CPW) circuit elements. The advantage of this planar design is that it can be fabricated directly on top of a crystalline substrate, in contrast to multilayer circuit elements, which generally make use of a deposited dielectric. Deposited amorphous dielectrics contain two-level system (TLS) defects that introduce dielectric loss and frequency noise.[5–7] However, multilayer circuit elements offer various benefits over planar circuit elements. The size of an MKID could be drastically reduced with a multilayer design, and microstrip filters suffer negligible radiation loss compared to planar filters.[8,9]

The peak transmission $|S_{31}|^2$ through a single isolated mm-submm filter[10,11] is

$$|S_{31}|^2 = \frac{1}{2}\left(1 - \frac{R}{Q_i}\right)^2, \tag{1}$$

*Address all correspondence to Bruno T. Buijtendorp, b.t.buijtendorp@tudelft.nl

where $R = F/\Delta F$ is the resolving power and Q_i is the internal quality factor. The $1/Q_i$ is roughly equal to the dielectric loss tangent in the case of a superconducting microstrip filter.[11–13] An increase in Q_i will enable a proportional increase in R at a particular filter transmission value.

A mm-submm Q_i of 1440 has been achieved with amorphous silicon nitride (SiN_x).[11] Recently, Q_i values of 4800 and 8300 were reported for hydrogenated amorphous silicon (a-Si:H)[12] and hydrogenated amorphous silicon carbide (a-SiC:H),[13] respectively. Further improvement in Q_i is desired to enable filters with higher R.

Although TLSs are successfully modeled by the standard tunneling model (STM),[5] their microscopic origin remains unknown. The TLSs dominate the dielectric loss in superconducting resonators at microwave frequencies.[7,12–15] In the STM the TLS density of states is frequency independent, and this leads to the suggestion that a decreased microwave loss translates to increased performance for the mm-submm filters. Currently, the best low-power microwave loss tangents $\tan\delta \sim 10^{-5}$ have been measured for a-Si:H films[7,12,14,15] and a-SiC:H films.[13]

Due to an observed relation between TLS density and atomic silicon density, it has been proposed that the TLSs in electron-beam evaporated amorphous silicon (a-Si) are related to voids in the material.[16] It was found that a very low void volume fraction can be achieved by depositing at elevated substrate temperatures T_{sub}.[16] Recently, it has been observed that although the TLS-induced internal friction in a-Si correlates with the atomic silicon density, the TLS-induced loss tangent instead correlates with the dangling bond density.[17]

In this work, we investigate the effect of T_{sub} on the microstructural and compositional properties of a-Si:H, and we study if these properties relate to the dielectric loss at 4 to 7 GHz and at 120 mK. For this purpose, we deposited a-Si:H films using plasma-enhanced chemical vapor deposition (PECVD) at three different substrate temperatures, and we measured their void volume fraction, hydrogen content, microstructure parameter, bond-angle disorder, and infrared (IR) refractive index.

2 Film Deposition

We deposited the a-Si:H films by PECVD with an Oxford Plasmalab 80 Plus. The substrate temperatures T_{sub} during the PECVD processes were 100°C, 250°C, and 350°C. The T_{sub} was the only parameter that was varied. The deposition parameters are listed in Appendix A. We used crystalline silicon (c-Si) substrates with (100) crystal orientation. Further substrate details and the wafer preparation details depend on the subsequent experiment and are described in the methods of each experiment. For the dielectric loss measurements, we used high resistivity wafers.

3 Characterization at Room Temperature

3.1 *Hydrogen Content, Microstructure Parameter, and Infrared Refractive Index*

The microstructure of a-Si:H is largely governed by the occurrence of SiH and SiH_2 configurations in the material.[18–20] The SiH configurations reside mostly in small vacancies, corresponding to up to three missing silicon (Si) atoms[19] per vacancy. This is in contrast to the SiH_2 configurations that exist mostly on the surface of voids with a radius of 1 to 4 nm, corresponding from 10^2 to 10^4 missing Si atoms[19] per void. We used Fourier-transform IR (FTIR) spectroscopy in transmission mode to measure the microstructure parameter R^* [Eq. (4)], which quantifies the relative amount of SiH and SiH_2 bonds. Using this method we also obtained the total hydrogen content C_H [Eq. (3)] of the films, and their IR refractive indices n_{ir}.

For the FTIR measurements, we deposited a-Si:H films on double side polished (DSP) p-type c-Si substrates with resistivity $\rho > 1$ kΩ cm. The substrates were dipped in 1% hydrofluoric acid for 1 min prior to film deposition.

By fitting the FTIR transmission data to a transfer-matrix method calculation[21] we obtained the n_{ir} and the absorption coefficients α of the a-Si:H films. In the fitting, we used a non-dispersive n_{ir}. We also measured the n_{ir} and α of the bare c-Si substrate, and used this to model the substrate in the calculation.

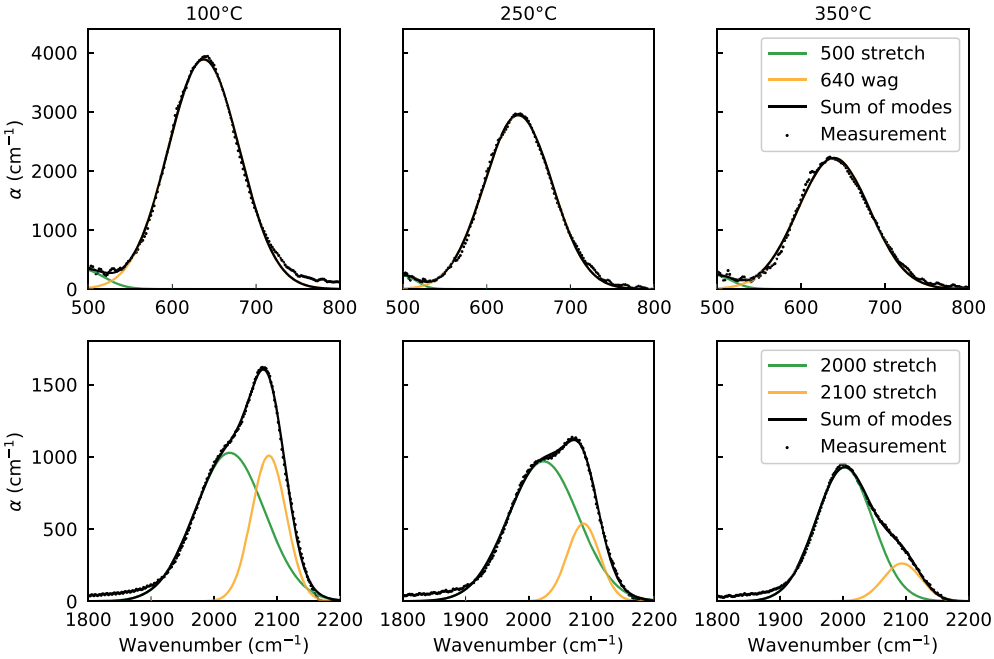

Fig. 1 The absorption coefficients α that we measured using FTIR spectroscopy, as a function of wavenumber. Each column shows the results for a particular film that was deposited at the substrate temperature T_{sub} shown on top. The top row shows the absorption near the wagging mode at 640 cm^{-1} (referred to as 640 wag), from which we calculated the hydrogen content C_H [Eq. (3)]. The bottom row shows the absorption near the stretching modes at 2000 and 2100 cm^{-1} (referred to as 2000 stretch and 2100 stretch), from which we calculated the microstructure parameter R^* [Eq. (4)].

The measured α and their Gaussian fits are plotted in Fig. 1. With increasing T_{sub}, we observe a decrease in intensity of the wagging mode near 640 cm^{-1} (referred to as 640 wag), indicating a decrease in the total hydrogen content.[18,22] We also observe an absorption peak near 500 cm^{-1} that can be attributed to a stretching mode[23] (referred to as 500 stretch). Also with increasing T_{sub}, we observe a decrease in intensity of the stretching mode near 2100 cm^{-1}, indicating a decrease in the amount of SiH_2 bonds.

To calculate the films' hydrogen contents C_H and their microstructure parameters R^* from the α spectra we numerically calculated the integrated absorptions I_x

$$I_x = \int \frac{\alpha_x(\tilde{\nu})}{\tilde{\nu}} \mathrm{d}\tilde{\nu}, \tag{2}$$

where x denotes the center wavenumber of the Gaussian absorption peak that is being integrated. From I_{640} we calculated C_H in atomic percent (at. %)[18,19,22,24]

$$C_H = \frac{A_{640} I_{640}}{A_{640} I_{640} + N_{\text{Si}}}, \tag{3}$$

where A_{640} is a proportionality constant that is an inverse cross-section for photon absorption at this wavenumber. We used the value $A_{640} = 2.1 \cdot 10^{19}$ cm^{-2}.[22] For N_{Si}, the atomic density of silicon, we used the value $5 \cdot 10^{22}$ cm^{-3}. The modes near 2000 and 2100 cm^{-1} can be attributed to SiH and SiH_2, respectively.[18] The fraction of Si atoms that are bonded as SiH_3 is negligible below hydrogen concentrations of 40%.[25] The microstructure parameter R^* was defined as[18]

$$R^* = \frac{I_{2100}}{I_{2100} + I_{2000}}. \tag{4}$$

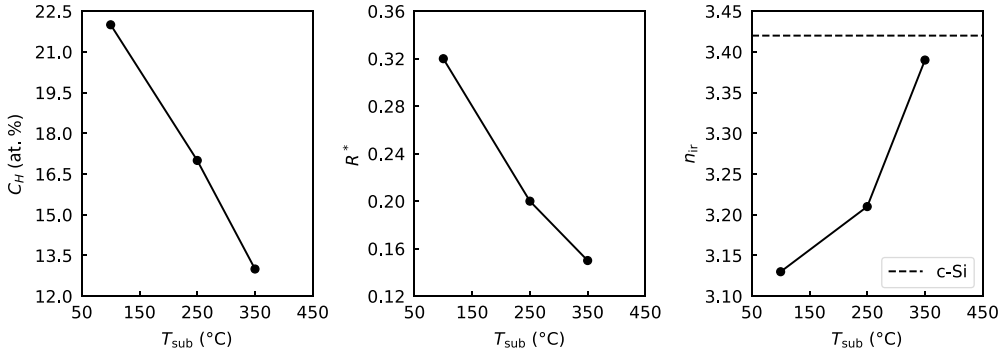

Fig. 2. The hydrogen contents C_H, microstructure parameters R^*, and IR refractive indices n_{ir} of the three films, which we derived from the FTIR data. The films were deposited at the substrate temperature T_{sub}. The dashed line in the right-most figure represents the literature value of the n_{ir} of c-Si.[22]

The results for the hydrogen content C_H, microstructure parameter R^*, and IR refractive index n_{ir} are plotted in Fig. 2. We observe that C_H decreases monotonically with increasing T_{sub}. The microstructure parameter R^* also decreases monotonically with increasing T_{sub}, indicating that a smaller fraction of the hydrogen is bonded in SiH_2 configurations, which reside mostly on the surface of voids.[19] Additionally, we observe that n_{ir} increases monotonically with increasing T_{sub}, indicative of an increase in film density.

3.2 *Bond-Angle Disorder*

Films of a-Si:H exhibit bond-angle disorder $\Delta\theta$ in their silicon network, defined as the root mean square deviation from the tetrahedral bond angle of 109.5 deg. We measured $\Delta\theta$ using Raman spectroscopy with a 514-nm laser[26]

$$\Delta\theta = \frac{505.5 - \tilde{\nu}_{TO}}{2.5}, \tag{5}$$

where $\tilde{\nu}_{TO}$ is the center wavenumber of the transverse-optic (TO) mode near 480 cm^{-1} (TO 480).

For Raman spectroscopy, we deposited the a-Si:H films on single side polished (SSP) n-type substrates with a resistivity ρ of $1-5\ \Omega$cm, and with a 101-nm thick thermal oxide layer.

In Fig. 3, we show the Raman measurement of the film deposited at 100°C, and the Gaussian fits. Apart from the TO 480 mode, we observe a transverse-acoustic (TA) mode near 170 cm^{-1} (TA 170),[27] a longitudinal-acoustic mode near 300 cm^{-1} (LA 300),[28] a longitudinal-optic mode near 425 cm^{-1} (LO 425), and at 520 cm^{-1} the TO mode of the c-Si substrate, fitted with a

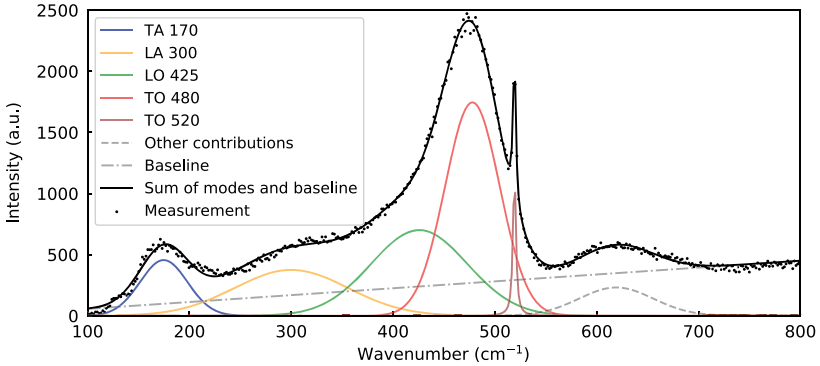

Fig. 3 The Raman spectroscopy measurement of the a-Si:H film that was deposited at a T_{sub} of 100°C. The plot serves to show the modes that are fitted to the measurement data. We calculated the bond-angle disorder $\Delta\theta$ from the position of the TO 480 mode.

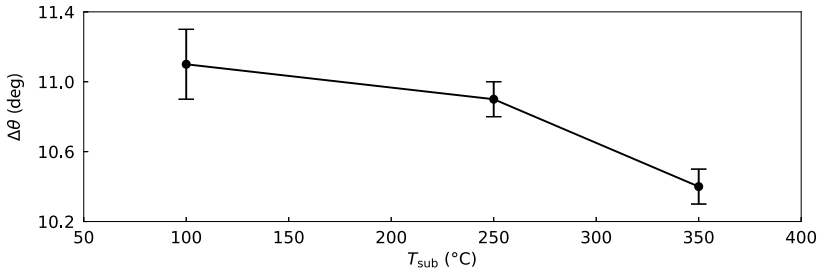

Fig. 4 The bond-angle disorder $\Delta\theta$ of the three a-Si:H films that we derived from the Raman spectroscopy measurements. The films were deposited at the substrate temperature T_{sub}. The error bars represent the standard deviations of $\Delta\theta$ that we estimated from the least-squares fit.

Lorentzian.[26,29] The peak near 620 cm^{-1} can be attributed to a variety of modes.[28–30] In our fit, we fixed the peak position of the LA 300 mode at 300 cm^{-1}.

We plot the measured $\Delta\theta$ of the three films in Fig. 4. We observe a monotonic decrease of $\Delta\theta$ with increasing T_{sub}.

3.3 *Void Volume Fraction*

We determined the films' void volume fractions f_v using variable-angle spectroscopic ellipsometry. The measured change in polarization was fitted to an optical model that includes a native oxide layer, the a-Si:H film, a thermal oxide layer, and the c-Si substrate. For this, we used the commercial software CompleteEASE.[31]

For ellipsometry, we deposited the a-Si:H films on SSP n-type substrates with a ρ of 1–5 $\Omega\,\text{cm}$, with a 101-nm thick thermal oxide layer for increased reflection.

We obtained f_v from the fit by using the Bruggeman effective medium approximation to model the a-Si:H film as a composite material consisting of a-Si and spherical voids.[13,32] The results for f_v are plotted in Fig. 5. We observe that f_v decreases monotonically with increasing T_{sub}.

4 Cryogenic Loss Tangent Measurement

4.1 *Method*

We fabricated superconducting chips with 109-nm-thick aluminum (Al) quarter-wavelength CPW resonators on top of the ~250-nm thick a-Si:H films. To estimate the losses other than the losses due to the a-Si:H we also fabricated a chip directly on top of a c-Si substrate. The Al layer was patterned using photolithography. We deposited the a-Si:H films on DSP intrinsic c-Si substrates with $\rho > 10\ \text{k}\Omega\,\text{cm}$. The substrates were dipped in 1% hydrofluoric acid for 1 min prior to film deposition.

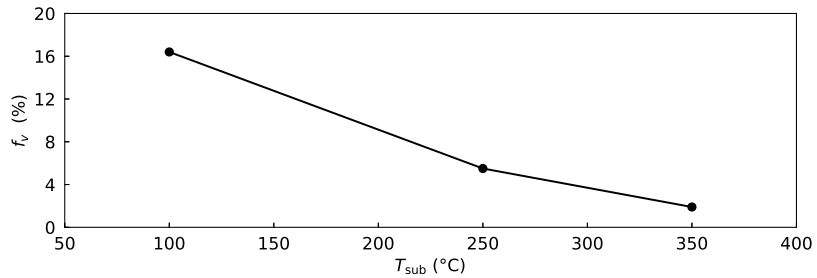

Fig. 5 The void volume fractions f_v of the three a-Si:H films, which we derived from the ellipsometry data by modeling the a-Si:H layer as a composite material of a-Si and spherical voids using the Bruggeman effective medium approximation. The films were deposited at the substrate temperature T_{sub}.

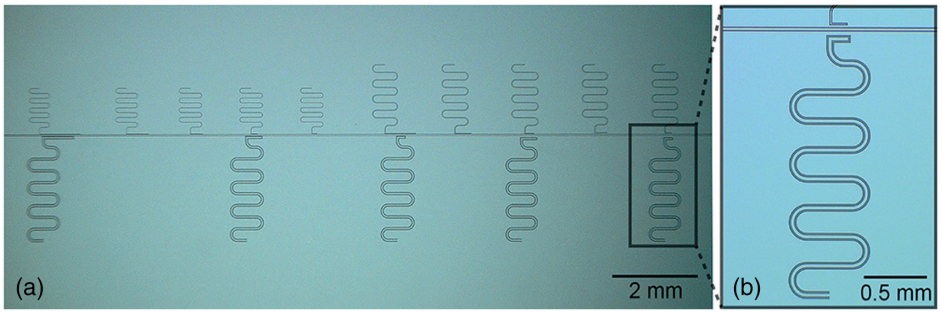

Fig. 6 (a) Micrograph of the superconducting chip. There are three groups of five quarter-wavelength CPW resonators, each group has a different CPW geometry (listed in Table 1). Within each group, the resonators vary in the coupling quality factor Q_c. (b) Zoomed-in micrograph of the bottom-right resonator in Fig. 6(a).

A micrograph of the chip with the 250°C a-Si:H is shown in Fig. 6(a). The chips feature a CPW readout line with a slot width s of 8 μm and a center line width c of 20 μm. The readout line is coupled to 15 resonators. The resonators are divided into three geometry groups with different s and c. The five resonators within each group have different coupling quality factors Q_c.

We obtained the loss tangents tan δ of the a-Si:H films at 4 to 7 GHz and at 120 mK. The cryogenic setup, which uses an adiabatic demagnetization refrigerator includes a 35-dB gain low noise (noise temperature of 3 to 4 K) high-electron-mobility transistor amplifier at the cryostat's 3-K stage, as well as two amplifiers at room temperature. The 120-mK stage is shielded from magnetic fields using a superconducting lead-tin coated shield that is surrounded by a Cryoperm shield. Further details on the cryogenic setup are given in De Visser's PhD thesis.[33] To derive tan δ, we measured the S-parameter $S_{21}(f)$ as a function of frequency using a vector network analyzer. We then obtained tan δ from $S_{21}(f)$ by fitting the squared magnitude of the measured $S_{21}(f)$ to a Lorentzian:

$$|S_{21}(f)|^2 = 1 - \frac{1 - S_{21,\min}^2}{1 + \left(2Q\frac{f-f_r}{f_r}\right)^2}. \tag{6}$$

Here, Q is the loaded quality factor, $S_{21,\min}$ is the minimum of the resonance dip, and f_r is the resonance frequency. The internal quality factor Q_i is determined from the equality[33]

$$Q_\mathrm{i} = Q/S_{21,\min}. \tag{7}$$

For each geometry group, we used the data of the resonator that was designed for the largest $Q_{c,\mathrm{design}} = 3 \times 10^5$ since these have the smallest fitting errors when fitting Eq. (6). The measured Q_c values vary between the different resonators in the range of $Q_c = 1.7$–3.3×10^5 and the values are listed in Appendix C. The $1/Q_i$ can be expressed as

$$\frac{1}{Q_i}(g) = p(g)\tan\delta + b(g), \tag{8}$$

where g makes it explicit that these quantities are dependent on the CPW geometry. The $p(g)$ is the filling fraction of the a-Si:H film (or the c-Si substrate in the case of the c-Si reference chip), which is the fraction of the resonator's electric energy that is stored inside the dielectric.[6] The $b(g)$ term in Eq. (8) represent the sum of all loss mechanisms other than the tan δ of the dielectric film. We calculated the $p(g)$ using the EM-solver Sonnet,[34] where we used the film thicknesses t_f (listed in Appendix B), which we measured using ellipsometry, and the ε_mw listed in Table 1. The resulting $p(g)$ are visible in Table 1.

Table 1 The filling fractions p of the a-Si:H films, which we calculated using the EM-solver Sonnet.[34] In the case of c-Si, the p is calculated for the substrate. The ε_{mw} of the a-Si:H films were estimated from their IR values as $\varepsilon_{mw} \approx (n_{ir}/n_{cSi,ir})^2 \varepsilon_{cSi,mw}$. In the heading, s is the CPW slot width and c is the CPW center line width.

	CPW s-c-s (μm)		
Material	2-3-2	6-9-6	18-27-18
c-Si ($\varepsilon_{mw} = 11.44$)	0.920	0.920	0.920
a-Si:H 100°C ($\varepsilon_{mw} \approx 9.5$)	0.208	0.101	0.044
a-Si:H 250°C ($\varepsilon_{mw} \approx 10.1$)	0.197	0.095	0.042
a-Si:H 350°C ($\varepsilon_{mw} \approx 11.2$)	0.214	0.103	0.045

From the STM, it follows that the TLS-induced tan δ is dependent on power, frequency, and temperature[6,17]

$$\tan\,\delta = \tan\,\delta_0\,\tanh\,\frac{\hbar\omega}{2k_BT}\left(1+\frac{N}{N_0}\right)^{-\beta/2}, \tag{9}$$

where tan δ_0 is the TLS-induced loss tangent at zero temperature and low internal resonator power, N is the average number of photons inside the resonator, N_0 is the critical photon number above which the TLSs start to saturate, and β is equal to 1 in the STM, but has experimentally been found to range between 0.3 and 0.7.[17] The frequency ω, the temperature T, and the photon number N are controlled by the experiment. We defined N as the average number of photons per quarter-wavelength, which is equal to $N = P_{int}/(2hf^2)$, where P_{int} is the internal resonator power, which can be calculated from the readout power.[6]

By equating the losses $b(g)$ from Eq. (8) to zero when deriving tan δ from $1/Q_i$ we calculate an upper bound of the tan δ of the dielectric under consideration. Additionally, we estimated the tan δ of the a-Si:H films by equating $b(g)$ to the $1/Q_i$ of the c-Si reference chip.

4.2 *Results*

In Fig. 7(a), we plot the measured Q_i versus N of the resonators. We observe that Q_i increases with increasing N and that it is dependent on the CPW geometry, even for the c-Si where the filling fraction of the c-Si substrate does not depend on the CPW geometry. The filling fractions of the dielectrics are listed in Table 1.

In Fig. 7(b), we show the upper bounds of the tan δ of the three a-Si:H films and of the c-Si substrate. The plotted tan δ take the filling fractions of the dielectrics into account [Eq. (8)]. We observe that the a-Si:H films have an order of magnitude higher upper bound of tan δ than the c-Si substrate. We do not observe a correlation between T_{sub} and the upper bound of tan δ. The upper bounds of tan δ vary with the CPW geometry. For each material, the lowest values for the upper bound of tan δ represent the overall upper bound since tan δ is independent of geometry. We plotted the overall upper bounds as lines in Fig. 7(b). These lines are fits to a power law. From the fits, we observe that the upper bound of the tan δ of the a-Si:H film that was deposited with a T_{sub} of 100°C has a steeper slope than the other two a-Si:H films.

The estimates of tan δ, which we calculated by using the $1/Q_i$ of the c-Si chip as an estimate for the losses other than the a-Si:H loss are plotted in Fig. 7(c). We do not observe a correlation between T_{sub} and the estimate of tan δ. The estimate of tan δ for each material varies with the CPW geometry.

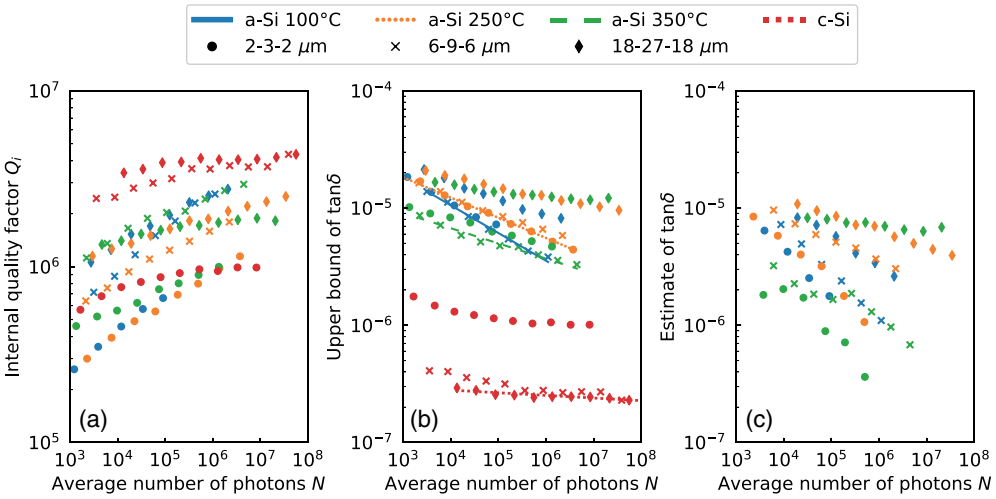

Fig. 7 (a) The measured internal quality factors Q_i of the resonators. The horizontal axis shows the average number of photons in the resonator per quarter-wavelength $N = P_{int}/(2hf^2)$, where P_{int} is the internal resonator power. (b) The upper bounds of tan δ, which we calculated by equating $b(g)$ in Eq. (8) to zero. The lines show the overall upper bounds of the tan δ of each material and are fits to a power law. (c) The estimates of tan δ which were calculated by equating $b(g)$ in Eq. (8) to the $1/Q_i$ of the c-Si reference chip, which has resonators directly on top of the c-Si substrate.

5 Discussion

Increasing T_{sub} results in films with less hydrogen, less voids, smaller microstructure parameter, less bond-angle disorder, and a higher IR refractive index and therefore higher film density. We have shown that changing T_{sub} is an effective way to monotonically control the structural and compositional properties of the a-Si:H. Interestingly, recent literature on electron-beam evaporated amorphous silicon suggests that the dielectric loss is correlated to the dangling bond density ρ_{DB}, which can be controlled by T_{sub}[17] as well.

Even though the structural and compositional properties at room temperature of the a-Si:H show a clear dependence on T_{sub}, we did not observe a correlation between tan δ and the room temperature properties or T_{sub}. At the powers at which we measured, a variation in the low-power TLS-induced loss tangent tan δ_0 cannot be distinguished from a variation in the critical photon number N_0, above which the TLSs start to saturate. However, if we assume that the three a-Si:H films have identical N_0, then the upper bounds of tan δ point to a low-power tan δ_0 that decreases monotonically with T_{sub}.

For the resonators with a-Si:H, it is expected that the Q_i is dependent on the CPW geometry due to differences in the dielectrics' filling fractions (Table 1). We observe that the Q_i of the c-Si resonators is also dependent on the CPW geometry even though the filling fraction of the c-Si substrate is equal for these resonators. We suggest that this is an effect due to TLS-hosting interface layers,[35–38] whose filling fractions and therefore effect on the measured tan δ are dependent on the CPW geometry. Furthermore, we suggest that the same effect causes the upper bound and the estimate of tan δ to be dependent on the CPW geometry, even though here the filling fractions of the dielectrics have been taken into account. Finally, we note that in reality the c-Si chip is not a perfect reference for the $b(g)$ term in Eq. (8), which results in some estimates being higher than the overall upper bound of tan δ [the lines in Fig. 7(b)]. This discrepancy can be explained by a different metal-dielectric surface, a different dielectric-air surface, and an additional surface between the a-Si:H film and the substrate that is not present on the c-Si chip.

The power and frequency range in which we measured is directly applicable to MKIDs, which operate at relatively high powers in comparison with the mm-submm filters that operate at single photon energies. The a-Si:H films are promising for MKID detectors because all three films exhibit an excellent tan $\delta < 10^{-5}$ at a resonator energy of 10^5 photons per quarter-wavelength, or at –55-dBm internal resonator power. Since the low microwave tan δ points to

a low TLS density, it is likely that the a-Si:H films also have low loss at mm-submm frequencies.[12] Finally, we note that a practical benefit of the a-Si:H film that was deposited at 250°C is that its stress σ is close to zero, as listed in Appendix B.

6 Conclusion

The structural and compositional room temperature properties of a-Si:H are monotonically controlled by changing the substrate temperature T_{sub} during deposition. We do not observe a correlation of the room temperature properties with tan δ. All three a-Si:H films exhibit a tan $\delta < 10^{-5}$ at 120 mK and at an average photon number N of 10^5, equivalent to –55-dBm internal resonator power. This makes these films promising for application in mm-submm on-chip filters and MKID detectors.

7 Appendix A: PECVD Deposition Parameters

This appendix provides the PECVD parameters which we used for the deposition of the a-Si:H films (Table 2).

Table 2 PECVD parameters.

Material	a-Si:H 100°C/250°C/350°C
T_{sub} (°C)	100/250/350
RF power (W)	15
SiH_4 flow (sccm)	25
Ar flow (sccm)	475
Pressure (Torr)	1
Deposition time (m′s″)	10′0″/7′9″/7′0″

8 Appendix B: Results of Characterization at Room Temperature

This appendix provides a summary of the results of the characterization at room temperature (Table 3).

Table 3 Results of the characterization at room temperature.

Film	a-Si:H 100°C	a-Si:H 250°C	a-Si:H 350°C
T_{sub} (°C)	100	250	350
C_H (at.%)	22	17	13
Microstructure parameter R^*	0.32	0.20	0.15
IR refractive index n_{ir}	3.13	3.21	3.39
Bond-angle disorder $\Delta\theta$	11.1 ± 0.2	10.9 ± 0.1	10.4 ± 0.1
Void volume fraction f_v (%)	16.5	5.6	2.0
Film thickness t_f (nm)	250.8 ± 0.1	236.0 ± 0.1	259.9 ± 0.1
Native oxide thickness t_n (nm)	5.8 ± 0.1	4.7 ± 0.1	4.2 ± 0.1
Stress σ (MPa) (tens.)	128.7	3.0	–379.0

9 Appendix C: Measured Coupling Quality Factors

This appendix provides the measured coupling quality factors of the resonators (Table 4).

Table 4 The coupling quality factors Q_c of the resonators, averaged over all readout powers. The listed uncertainties are the standard deviations in Q_c. In the heading, s is the CPW slot width and c is the CPW center line width.

	CPW s-c-s (μm)		
Material	2-3-2	6-9-6	18-27-18
c-Si	$2.83 \pm 0.04 \times 10^5$	$2.65 \pm 0.09 \times 10^5$	$1.96 \pm 0.03 \times 10^5$
a-Si:H 100°C	$1.67 \pm 0.01 \times 10^5$	$2.06 \pm 0.05 \times 10^5$	$2.00 \pm 0.06 \times 10^5$
a-Si:H 250°C	$1.76 \pm 0.02 \times 10^5$	$3.05 \pm 0.07 \times 10^5$	$3.13 \pm 0.11 \times 10^5$
a-Si:H 350°C	$3.32 \pm 0.04 \times 10^5$	$2.06 \pm 0.05 \times 10^5$	$2.98 \pm 0.10 \times 10^5$

Acknowledgments

The first author would like to express his gratitude toward Marco van der Krogt for helping with the deposition of the a-Si:H films. This paper was based on work that was reported in the conference proceedings of SPIE. 11453, Millimeter, Submillimeter, and Far-Infrared Detectors and Instrumentation for Astronomy X.[32] The contribution of J.J.A. Baselmans was supported by the ERC CoG 648135 MOSAIC.

References

1. J. Wheeler et al., "SuperSpec, the on-chip spectrometer: improved NEP and antenna performance," *J. Low Temp. Phys.* **193**, 408–414 (2018).
2. G. Cataldo et al., "Second-generation design of micro-spec: a medium-resolution, sub-millimeter-wavelength spectrometer-on-a-chip," *J. Low Temp. Phys.* **193**, 923–930 (2018).
3. A. Endo et al., "First light demonstration of the integrated superconducting spectrometer," *Nat. Astron.* **3**, 989–996 (2019).
4. P. K. Day et al., "A broadband superconducting detector suitable for use in large arrays," *Nature* **425**, 817–821 (2003).
5. W. A. Phillips, "Tunneling states in amorphous solids," *J. Low Temp. Phys.* **7**, 351–360 (1972).
6. J. Gao, "The physics of superconducting microwave resonators," PhD thesis, California Institute of Technology (2008).
7. A. D. O'Connell et al., "Microwave dielectric loss at single photon energies and millikelvin temperatures," *Appl. Phys. Lett.* **92**, 112903 (2008).
8. A. Endo et al., "Wideband on-chip terahertz spectrometer based on a superconducting filter-bank," *J. Astron. Telesc. Instrum. Syst.* **5**(3), 035004 (2019).
9. S. Hähnle et al., "Suppression of radiation loss in high kinetic inductance superconducting co-planar waveguides," *Appl. Phys. Lett.* **116**(18), 182601 (2020).
10. A. Endo et al., "On-chip filter bank spectroscopy at 600-700 GHz using NbTiN superconducting resonators," *Appl. Phys. Lett.* **103**(3) (2013).
11. S. Hailey-Dunsheath et al., "Optical measurements of SuperSpec: a millimeter-wave on-chip spectrometer," *J. Low Temp. Phys.* **176**(5–6), 841–847 (2014).
12. S. Hähnle et al., "Superconducting microstrip losses at microwave and submillimeter wavelengths," *Phys. Rev. Appl.* **16**(1), 014019 (2021).
13. B. T. Buijtendorp et al., "Hydrogenated amorphous silicon carbide: a low-loss deposited dielectric for microwave to submillimeter wave superconducting circuits," arXiv: 2110.03500 (2021).

14. B. A. Mazin et al., "Thin film dielectric microstrip kinetic inductance detectors," *Appl. Phys. Lett.* **96**, 102504 (2010).
15. A. Bruno et al., "Investigation of dielectric losses in hydrogenated amorphous silicon (a-Si:H) thin films using superconducting microwave resonators," *Phys. Proc.* **36**, 245–249 (2012).
16. D. Queen et al., "Two-level systems in evaporated amorphous silicon," *J. Non-Cryst. Solids* **426**, 19–24 (2015).
17. M. Molina-Ruiz et al., "Origin of mechanical and dielectric losses from two-level systems in amorphous silicon," *Phys. Rev. Mater.* **5**(3), 035601 (2020).
18. J. D. Ouwens and R. E. I. Schropp, "Hydrogen microstructure in hydrogenated amorphous silicon," *Phys. Rev. B* **54**, 17759–17762 (1996).
19. A. H. M. Smets, W. M. M. Kessels, and M. C. M. van de Sanden, "Vacancies and voids in hydrogenated amorphous silicon," *Appl. Phys. Lett.* **82**, 1547–1549 (2003).
20. W. Beyer et al., "Voids in hydrogenated amorphous silicon materials," *J. Non-Cryst. Solids* **358**, 2023–2026 (2012).
21. S. J. Byrnes, "TMM documentation," https://pythonhosted.org/tmm/tmm.html.
22. A. A. Langford et al., "Infrared absorption strength and hydrogen content of hydrogenated amorphous silicon," *Phys. Rev. B* **45**, 13367–13377 (1992).
23. N. Maley, "Critical investigation of the infrared-transmission-data analysis of hydrogenated amorphous silicon alloys," *Phys. Rev. B* **46**, 2078–2085 (1992).
24. R. Street, *Hydrogenated Amorphous Silicon*, Cambridge Solid State Science Series, Cambridge University Press (1991).
25. K. Mui and F. W. Smith, "Optical dielectric function of hydrogenated amorphous silicon: Tetrahedron model and experimental results," *Phys. Rev. B* **38**, 10623–10632 (1988).
26. R. L. C. Vink, G. T. Barkema, and W. F. van der Weg, "Raman spectra and structure of amorphous Si," *Phys. Rev. B* **63**, 115210 (2001).
27. D. J. Lockwood and A. Pinczuk, Eds., *Optical Phenomena in Semiconductor Structures of Reduced Dimensions*, Springer Netherlands, Dordrecht (1993).
28. M. H. Brodsky, M. Cardona, and J. J. Cuomo, "Infrared and Raman spectra of the silicon-hydrogen bonds in amorphous silicon prepared by glow discharge and sputtering," *Phys. Rev. B* **16**, 3556–3571 (1977).
29. C. Smit et al., "Determining the material structure of microcrystalline silicon from Raman spectra," *J. Appl. Phys.* **94**, 3582–3588 (2003).
30. P. Mishra and K. P. Jain, "First- and second-order Raman scattering in nanocrystalline silicon," *Phys. Rev. B* **64**, 073304 (2001).
31. J. A. Woollam, "CompleteEASE," https://www.jawoollam.com/ellipsometry-software/completeease.
32. B. T. Buijtendorp et al., "Characterization of low-loss hydrogenated amorphous silicon films for superconducting resonators," *Proc. SPIE* **11453**, 459–472 (2020).
33. P. De Visser, "Quasiparticle dynamics in aluminium superconducting microwave resonators," PhD thesis, Delft University of Technology (2014).
34. Sonnet, "Sonnet user's guide," http://www.sonnetsoftware.com/support/manuals.asp.
35. J. Gao et al., "Experimental evidence for a surface distribution of two-level systems in superconducting lithographed microwave resonators," *Appl. Phys. Lett.* **92**, 152505 (2008).
36. J. Wenner et al., "Surface loss simulations of superconducting coplanar waveguide resonators," *Appl. Phys. Lett.* **99**(11), 113513 (2011).
37. W. Woods et al., "Determining interface dielectric losses in superconducting coplanar-waveguide resonators," *Phys. Rev. Appl.* **12**(1), 1 (2019).
38. R. Barends et al., "Reduced frequency noise in superconducting resonators," *Appl. Phys. Lett.* **97**(3), 033507–2011 (2010).

Bruno T. Buijtendorp is a PhD candidate at Delft University of Technology (TU Delft), in the Terahertz Sensing Group. He received his BSc and MSc degrees in applied physics from TU Delft. His research focuses on improving and understanding the dielectric loss and noise in superconducting resonators, mainly in the context of astronomical detectors.

Juan Bueno graduated in physics from the University of Cantabria in 2003 and received his PhD from the University of Leiden in 2007. In 2008, he was awarded with a NASA postdoctoral position, joining the Jet Propulsion Laboratory. He became an instrument scientist at SRON in 2012 working on the development of far-IR and sub-mm wave kinetic inductance detectors. He is currently a high frequency RF engineer at TU Delft since 2021.

David J. Thoen is a cleanroom engineer working at TU Delft. He received his BSc degree (Hon, 2008) in applied physics from Fontys University of Applied Sciences, Eindhoven, while he worked as a microwave engineer at FOM Institute Rijnhuizen (now DIFFER) since 2007. Since 2010, he has worked at TU Delft on the development of microwave kinetic inductance detectors (MKID) far-infrared detectors for astronomy. He has extensive experience in cleanroom processing, process development, vacuum, and cryogenic technology.

Vignesh Murugesan is a process development engineer at SRON Netherlands Institute for Space Research. He is currently responsible for the process development and microfabrication of superconducting detectors. He received his MSc degree in microsystem integration technology from the Chalmers University of Technology in 2007. He worked as a process integration engineer from 2007 to 2008 for Infineon Technologies AG. From 2010 to 2013, he worked as a MEMS process engineer for Thermo Fisher Scientific.

Paolo M. Sberna received his BSc and MSc degrees in physics (cum laude) from the University of Catania, Italy. He got the PhD from the same university with a thesis on metal oxides semiconductors for thin-film solar cells. He currently works at TU Delft (The Netherlands) as a senior researcher with main focus on: photo-detectors, theory of hetero-junctions, photo-conductive antennas for THz and MEMS.

Jochem J. A. Baselmans is a senior instrument scientist at the SRON Netherlands Institute for Space Research and full professor in the THz sensing group at TU Delft. He leads the Dutch effort on the development of MKIDs, where his main interests are ultra-sensitive devices for THz radiation detection and advanced on-chip imaging spectrometers for sub-THz imaging spectroscopy.

Sten Vollebregt received his MSc (cum laude) and PhD degrees in electrical engineering from TU Delft in 2009 and 2014, respectively. Since October 2017, he has been an assistant professor with the Microelectronics Department, TU Delft. His research focuses on the integration of emerging electronic materials into semiconductor technology for sensing applications. His research interests include (carbon-based) nanomaterials, 3D monolithic integration, wide-bandgap semiconductors, and (harsh) environmental sensors.

Akira Endo is an assistant professor at the THz Sensing Group of TU Delft. He is interested in 3D-observations of large cosmological volumes, and the required development of (sub)millimeter-wave integral field units. He is the Dutch PI of the wideband DESHIMA spectrometer on the ASTE telescope. In 2022, he received his ERC Consolidator Grant to develop integral field units with many spaxels, and to demonstrate it with astronomical observations (project TIFUUN).